

Article

Actual Evapotranspiration (Water Use) Assessment of the Colorado River Basin at the Landsat Resolution Using the Operational Simplified Surface Energy Balance Model

Ramesh K. Singh ^{1,*}, Gabriel B. Senay ², Naga M. Velpuri ¹, Stefanie Bohms ³, Russell L. Scott ⁴ and James P. Verdin ²

¹ ASRC Federal InuTeq, Contractor to the US Geological Survey Earth Resources Observation and Science Center, 47914 252nd Street, Sioux Falls, SD 57198, USA; E-mail: nvelpuri@usgs.gov

² US Geological Survey Earth Resources Observation and Science Center, 47914 252nd Street, Sioux Falls, SD 57198, USA; E-Mails: senay@usgs.gov (G.B.S.); verdin@usgs.gov (J.P.V.)

³ Stinger Ghaffarian Technologies Inc., Contractor to the US Geological Survey Earth Resources Observation and Science Center, Sioux Falls, SD 57198, USA; E-Mail: sbohms@usgs.gov

⁴ Southwest Watershed Research Center, US Department of Agriculture, Tucson, AZ 85719, USA; E-Mail: russ.scott@ars.usda.gov

* Author to whom correspondence should be addressed; E-Mail: rsingh@usgs.gov; Tel.: +1-605-594-2751; Fax: +1-605-594-6529.

Received: 10 November 2013; in revised form: 28 November 2013 / Accepted: 16 December 2013 / Published: 20 December 2013

Abstract: Accurately estimating consumptive water use in the Colorado River Basin (CRB) is important for assessing and managing limited water resources in the basin. Increasing water demand from various sectors may threaten long-term sustainability of the water supply in the arid southwestern United States. We have developed a first-ever basin-wide actual evapotranspiration (ET_a) map of the CRB at the Landsat scale for water use assessment at the field level. We used the operational Simplified Surface Energy Balance (SSEBop) model for estimating ET_a using 328 cloud-free Landsat images acquired during 2010. Our results show that cropland had the highest ET_a among all land cover classes except for water. Validation using eddy covariance measured ET_a showed that the SSEBop model nicely captured the variability in annual ET_a with an overall R^2 of 0.78 and a mean bias error of about 10%. Comparison with water balance-based ET_a showed good agreement ($R^2 = 0.85$) at the sub-basin level. Though there was good correlation ($R^2 = 0.79$) between Moderate Resolution Imaging Spectroradiometer (MODIS)-based ET_a (1 km spatial resolution) and Landsat-based ET_a (30 m spatial resolution), the spatial distribution of

MODIS-based ET_a was not suitable for water use assessment at the field level. In contrast, Landsat-based ET_a has good potential to be used at the field level for water management. With further validation using multiple years and sites, our methodology can be applied for regular production of ET_a maps of larger areas such as the conterminous United States.

Keywords: evapotranspiration; energy balance; geospatial analysis; hydrologic cycle; irrigation; Landsat; remote sensing; water use

1. Introduction

Water management is becoming more challenging, particularly in the arid western United States because of changes in climate, land use, and demography. One climate change study has indicated that annual runoff in the Colorado River Basin (CRB) will be reduced by 14%, 18%, and 17% for the periods 2010–2039, 2040–2069, and 2070–2098, respectively [1]. The reduced availability of water in the basin could also prevent water allocation requirements of the Colorado River Compact from being met [2]. Increased demand for water from various sectors has motivated water managers to demand more accurate water budgets at higher resolution so that available water resources may be better allocated.

Remote sensing has great potential but remains underutilized by practicing water resource managers [3,4]. Accurately estimating consumptive water use using remotely sensed data helps water managers in planning, distribution, and management of water resources. Agro-meteorological models based on remote sensing are the most suited for estimating crop water use at the field and regional scales [5]. Some of the remote sensing based models for estimating actual evapotranspiration (ET_a) include the surface energy balance index (SEBI) [6], two source model (TSM) [7], surface energy balance algorithm for land (SEBAL) [8], simplified surface energy balance index (S-SEBI) [9], surface energy balance system (SEBS) [10], ET mapping algorithm (ETMA) [11], atmosphere-land exchange inverse (ALEXI) [12], mapping evapotranspiration at high resolution with internalized calibration (METRIC) [13], simplified surface energy balance (SSEB) [14], wet METRIC (wMETRIC) [15], and operational simplified surface energy balance (SSEBop) [16]. Various publications have reviewed some of these models and other methods for estimating ET_a using remotely sensed data [5,17–19].

The US Bureau of Reclamation of the Department of the Interior (DOI) is the nodal agency for managing water in the Colorado River Basin. As per “the 1964 Decree” of the U.S. Supreme Court in *Arizona vs. California et al.*, the Secretary of the DOI must provide complete, detailed, and accurate records of consumptive use of water from the Colorado River. Furthermore, one of the six science strategic directions of the US Geological Survey (USGS) in the decade 2007–2017 is a Water Census (water availability and use assessment) of the United States for quantifying, forecasting, and securing freshwater for America’s future [20]. The DOI has launched WaterSMART (Sustain and Manage America’s Resources for Tomorrow) to achieve a sustainable water strategy to meet the Nation’s water needs [21]. The CRB is one of the focus areas under WaterSMART initiatives for developing and testing suitable methods to meet the Water Census objectives [22].

Our objective of this study is to produce seamless ET_a estimates of the Colorado River Basin at the Landsat scale using the SSEBop model and evaluate the model performance using field measurements, water balance study, and Moderate Resolution Imaging Spectroradiometer (MODIS)-based ET_a estimates.

2. Methods and Materials

The operational Simplified Surface Energy Balance (SSEBop) model was used for estimating ET_a within the CRB. This model uses pre-defined hot and cold boundary conditions unique to each pixel. Independent weather datasets from the Global Data Assimilation System (GDAS) are used to compute the reference ET (ET_o). ET_o is constrained by ET fraction (ET_f) based on Landsat surface temperature and Parameter-Elevation Regressions on Independent Slopes Model (PRISM) air temperature data. A brief overview of the SSEBop model is presented here. Readers may refer to Senay *et al.* (2013) [16] for more details on model parameterization, hypothesis, and justification.

2.1. The Operational Simplified Surface Energy Balance (SSEBop) Model

The SSEBop Model uses a pre-defined hot and cold boundary condition for computing daily evapotranspiration ET_a ($\text{mm}\cdot\text{d}^{-1}$) as

$$ET_a = ET_f \times k \times ET_o \quad (1)$$

where ET_o is short grass reference ET ($\text{mm}\cdot\text{d}^{-1}$), ET_f is ET fraction (-), and k is a scaling coefficient (-) based on calibration. In this study we used k as 1. Senay *et al.* (2013) [16] suggest a calibration process to determine the k value since the calculation of the pre-defined parameters may already incorporate a compensating bias.

ET fraction, ET_f (-), is computed as

$$ET_f = \frac{T_h - T_s}{T_h - T_c} \quad (2)$$

where T_h is pre-defined idealized reference hot pixel temperature (K), T_s is land surface temperature (K) obtained from Landsat images, and T_c is pre-defined idealized reference cold pixel temperature (K).

In the SSEBop model, each pixel has a predefined hot and cold boundary values based on maximum air temperature and differential temperature (dT). Pre-defined cold pixel temperature is computed as a fraction of maximum air temperature. Maximum air temperature is not selected over the Landsat scene or the modeling domain but each pixel has its own predefined boundary values. The cold pixel temperature is approximated as being close to the corresponding air temperature based on the assumption that for a given clear-sky day, the land surface will experience an ET_a rate equal to the potential rate for healthy and well watered vegetation when its T_s is close to the near-surface air temperature (*i.e.*, little or no sensible heat flux). Calibration of the SSEBop Model using MODIS-based images has shown this coefficient as 0.993 [16]. However, our calibration using Landsat images has shown a different value; hence, we computed T_c as

$$T_c = 0.985 \times T_{max} \quad (3)$$

where T_{max} is the maximum air temperature (K).

Pre-defined hot pixel temperature is computed as

$$T_h = T_c + dT \quad (4)$$

Differential temperature (dT , K) is computed based on the assumption that latent heat flux and heat storage at the daily time scale for a dry, bare soil will be negligible. Thus based on energy balance, sensible heat flux (H) will be equal to net radiation (R_n) at the dry, bare soil. So we can replace H with R_n in the conventional H formulation and compute dT as

$$dT = \frac{R_n \times r_{ah}}{\rho_a \times c_p} \quad (5)$$

where r_{ah} is the aerodynamic resistance to heat transfer from a hypothetical dry, bare surface ($110 \text{ s}\cdot\text{m}^{-1}$), ρ_a is the density of air ($\text{kg}\cdot\text{m}^{-3}$), and c_p is the specific heat of air at constant pressure ($1,004 \text{ J}\cdot\text{kg}^{-1}\cdot\text{K}^{-1}$). The calculations of net radiation (R_n) under clear-sky condition and air density (ρ_a) are adaptations of Allen *et al.* (1998) [23] as described in Senay *et al.* [16]. It is important to note that dT is unique for each period and location, but the value does not vary from year to year since it is calculated under a clear-sky condition.

2.2. Study Area

The Colorado River originates in the Rocky Mountains of the western United States and flows about 2,300 km through seven states (Wyoming, Colorado, Utah, New Mexico, Arizona, Nevada, and California) before draining into the Gulf of California (Figure 1). The CRB has an area of about 630,000 km^2 , much of it arid. The Colorado River is a major source of water supply to the southwestern United States. The Colorado River supplies water to more than 25 million people and irrigates more than 12,000 km^2 of cropland across the seven basin states [22]. The annual flow of the river has ranged from 6.5 billion cubic meters (BCM) to 29.6 BCM during 1906–2000 [1]. The combined reservoir storage capacity (74.0 BCM) within the basin is about four times the long-term average annual flow (16.7 BCM).

Figure 1. Location of the study area showing the Colorado River Basin.

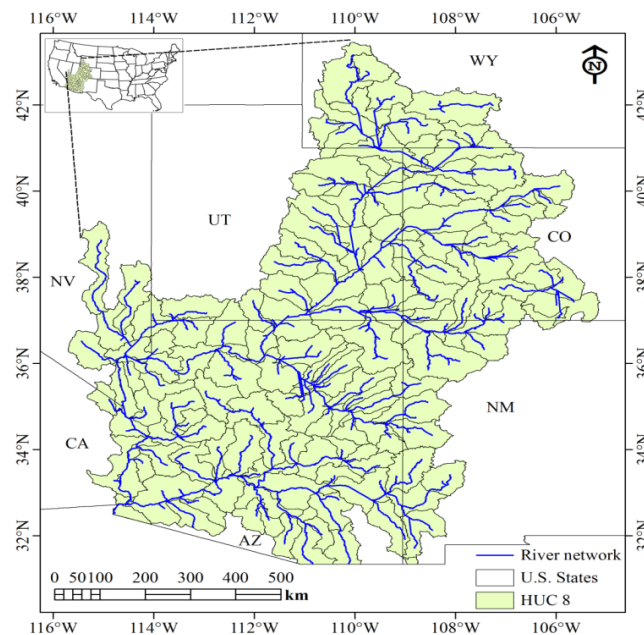
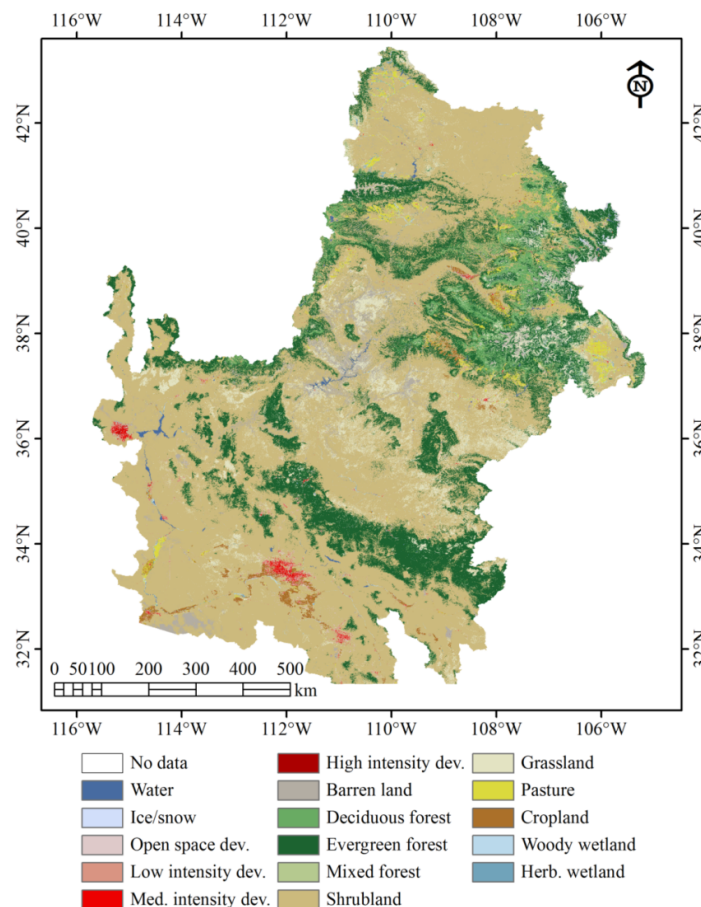


Table 1. Land use/land cover distribution within the study area based on National Land Cover Database [24].

Land Use/Land Cover	NLCD Code	%
Water	11	0.40
Ice/snow	12	0.05
Open space development	21	0.79
Low intensity development	22	0.51
Med. intensity development	23	0.24
High intensity development	24	0.05
Barren land	31	3.34
Deciduous forest	41	3.51
Evergreen forest	42	19.35
Mixed forest	43	0.38
Shrubland	52	60.56
Grassland	71	7.73
Pasture/Hay	81	1.44
Cropland	82	0.83
Woody Wetland	90	0.58
Herbaceous Wetland	95	0.22

Figure 2. Land use/land cover distribution in the Colorado River Basin based on National Land Cover Database 2006 [24].

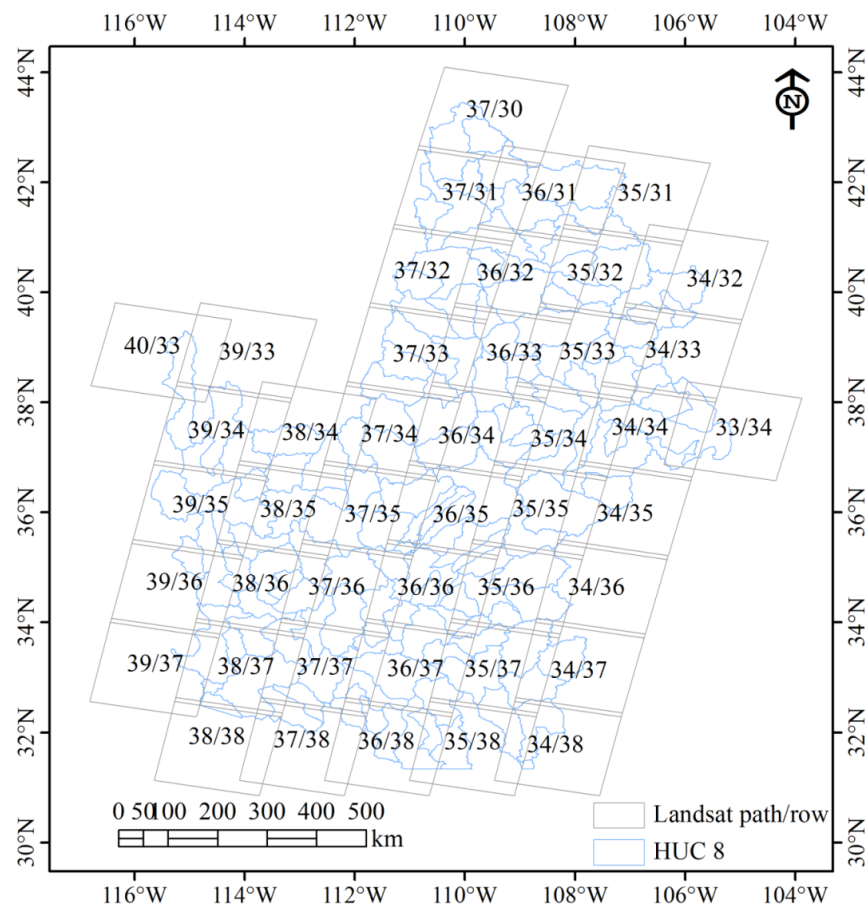


Based on the National Land Cover Database (NLCD, 2006) [24], shrubland (61%) is the most dominant land cover in the study area followed by evergreen forest (19%) (Table 1). Most of the pastureland is in the upper basin, most of the cropland is in the lower basin, and shrubland is distributed throughout the basin (Figure 2). Land use/land cover of the CRB is also used as an input in the Lower Colorado River Accounting System (LCRAS), a water accounting system developed by the USGS and the Bureau of Reclamation [25]. Congalton *et al.* (1998) [26] developed a procedure to accurately map agricultural crops and other land cover in the lower CRB. For additional detail on geo-topographic and climatic conditions of the study area, see Kumar and Duffy (2009) [27].

2.3. Processing of Landsat Images

The CRB is covered by 44 Landsat scenes spread over paths 33–44 and rows 30–38 (Figure 3). First, we downloaded all the Landsat images (Thematic mapper and Enhanced thematic mapper plus) of the study area for 2010 with less than 10% cloud cover from the Earth Explorer site (<http://earthexplorer.usgs.gov/>). We then selected images that were nearly cloud free or had cloud only along the edges (total 328 images). In general, one Landsat image per month is ideal, but two images are desired for cropland, particularly during the crop growing season. However, based on our Landsat processing experience, reasonable results can be obtained based on 10–12 images per year.

Figure 3. Coverage of Landsat TM/ETM+ images (path/row) in the Colorado River Basin based on the worldwide reference system (WRS-2).



Processing of Landsat images for obtaining land surface temperature (T_s) was carried out as follows. First, the digital numbers (DN) of downloaded Landsat images were converted to at-sensor radiance (L) as

$$L = \frac{(L_{\max} - L_{\min}) \times (DN - Q_{cal\min})}{(Q_{cal\max} - Q_{cal\min})} + L_{\min} \quad (6)$$

where L is spectral radiance ($\text{W} \cdot \text{m}^{-2} \cdot \text{sr}^{-1} \cdot \mu\text{m}^{-1}$), L_{\max} is maximum rescaling factor ($\text{W} \cdot \text{m}^{-2} \cdot \text{sr}^{-1} \cdot \mu\text{m}^{-1}$), L_{\min} is minimum rescaling factor ($\text{W} \cdot \text{m}^{-2} \cdot \text{sr}^{-1} \cdot \mu\text{m}^{-1}$), DN is quantized calibrated pixel value (-), $Q_{cal\max}$ is quantized calibrated pixel value corresponding to the L_{\max} (-), and $Q_{cal\min}$ is quantized calibrated pixel value corresponding to the L_{\min} (-). The values of L_{\max} , L_{\min} , $Q_{cal\max}$, and $Q_{cal\min}$ for each band are provided in the metafile of unzipped downloaded images.

The at-sensor radiance for the shortwave bands was converted to top of atmosphere reflectance (ρ) as

$$\rho = \frac{\pi \times L}{ESUN \times \cos\theta \times d_r} \quad (7)$$

where ρ is planetary top of atmosphere reflectance (-), d_r is earth-sun distance parameter (-), $ESUN$ is mean exoatmospheric solar irradiance ($\text{W} \cdot \text{m}^{-2} \cdot \mu\text{m}^{-1}$), and θ is solar zenith angle (degree). $ESUN$ values are given in Chander *et al.* (2009) [28].

Top of atmosphere albedo and at surface albedo were calculated as

$$\alpha_{toa} = \sum (\rho \times c) \quad (8)$$

$$\alpha = \frac{\alpha_{toa} - \alpha_{path}}{\tau_{sw}^2} \quad (9)$$

where α_{toa} is albedo at the top of the atmosphere (-), α is at surface albedo (-), c is weighting coefficient (based on Tasumi *et al.*, 2008) [29], α_{path} is albedo path radiance ranging from 0.025 to 0.04 (-), and τ_{sw} is transmittance as computed below.

$$\tau_{sw} = 0.75 + 2 \times 10^{-5} \times Z \quad (10)$$

where Z is elevation above the mean sea level (m).

Surface emissivity and land surface temperature were computed as presented in Allen *et al.* (2007) [13] without using any atmospheric radiative transfer simulation model such as MODTRAN. In some desert areas where albedo is high (>0.3), the radiometric land surface temperature tends to decrease, potentially due to reduced net radiation [16]. We corrected those T_s values to avoid erroneous ET fraction as

$$T_{s_co} = T_s + 50 \times (\alpha - 0.3) \quad (11)$$

where T_{s_co} is corrected land surface temperature (K).

The SSEBop model algorithm was implemented with Landsat images using Model Maker in Erdas Imagine 2011 (version 11.0.4) (Intergraph Corporation, Huntsville, AL, USA). Each individual scene was processed separately for computing ET_a on the day of the satellite overpass. All the available daily ET_a images were used for upscaling to compute annual ET_a as discussed in the Computation of Annual ET section.

2.4. Other Supporting Data

Monthly minimum and maximum temperature and precipitation (P) gridded 4 km data for 2010 were downloaded from the Parameter-Elevation Regressions on Independent Slopes Model (PRISM) website. We used these data in their original format without any spatial interpolation to preserve the data integrity. PRISM is a knowledge-based system that uses ground-based meteorological station records, a digital elevation model (DEM), and many other geographic datasets to generate gridded estimates of monthly climatic parameters [30]. Monthly runoff (Q) based on Hydrologic Unit Code (HUC) for 2010 was downloaded from the USGS Water Watch website (<http://waterwatch.usgs.gov/index.php>). The estimates of HUC runoff are generated by the USGS by combining historical flow data from stream gauges, the drainage basins of the stream gauges, and the HUC boundaries [31]. Annual ET_a based on spatial water balance at the HUC8 level was carried out by subtracting annual HUC-based runoff from the annual PRISM precipitation. Only PRISM-based air temperature (not precipitation) was used in the SSEBop model for computing Landsat-based ET_a . Thus ET_a based on water balance (residual of precipitation and runoff, *i.e.*, $P-Q$) should serve as an independent data source for validation of Landsat-based annual ET_a . We assume that there is no change in annual storage of water; therefore, $P-Q$ is equivalent to ET_a .

Topographic elevation data of the study area were derived from the February 2000 National Aeronautics and Space Administration (NASA) Shuttle Radar Topography Mission (SRTM), a seamless and complete void-filled spatial dataset [32]. Data were downloaded from the SRTM data portal. The daily reference evapotranspiration (ET_o) (Senay *et al.*, 2008) [33] was computed from climate parameter data extracted from global data assimilation system (GDAS) based 6-hourly weather datasets [34]. The daily ET_o data are available at the Famine Early Warning Systems Network website (<http://earlywarning.usgs.gov/adds/global/index.php>). The global ET_o data available at 1° ground resolution were downscaled to 10 km resolution [14]. Gridded flux data are a global, spatially and temporally explicit estimates of latent flux upscaled from flux measurements based on remote sensing indices, climate and meteorological data, and information on land use [35]. These data were obtained from the Max Planck Institute for Biogeochemistry server. MODIS-based ET_a maps using the SSEBop model [16] were also used for result comparison.

2.5. Computation of Annual Evapotranspiration

ET_a on the day of the satellite overpass was computed using the SSEBop model. Computation of seasonal/annual ET_a becomes challenging when daily ET_a is not available because of Landsat's 16-day repeat cycle and/or a lack of cloud-free images. We have used upscaling of daily ET_a to annual ET_a based on the ratio of actual ET to reference ET (ET coefficient). A study by Singh (2009) [36] with multiyear datasets showed that there was no single interpolation method that worked better than other methods under all conditions. Suitability of the method depended on the number of images per season, number of days between two consecutive images, extreme values on any particular day, and duration of the season [37]. The fixed method worked well for longer duration (annual). So we used the fixed method for computing annual ET based on ET coefficient:

$$ET_{annual} = \sum_{i=1}^n (ET_{oi} \times ET_{fi}) \quad (12)$$

where ET_{annual} is the total annual ET (mm), ET_{oi} is the reference ET (mm) for period i (days), and ET_{fi} is the representative ET coefficient (–) for period i .

After computing the annual ET_a for each path/row, all annual ET_a images were mosaicked. Mosaicking of annual ET_a for different path/row is done to obtain a nearly seamless ET_a map. For this we used average values for the overlapped area. Finally, the study area was extracted from the mosaicked images using a boundary shape file of the river basin.

2.6. Field Validation

Modeled ET_a was compared with the eddy covariance measurements carried out at the different eddy covariance measurement sites (Table 2). These sites are Flagstaff managed forest [38], Flagstaff unmanaged forest [38], Flagstaff wildfire [38], Santa Rita Creosote [39], Santa Rita Mesquite [40], Kendall grassland [41], and Charleston Mesquite [42]. For comparison, we used the ET_a values of pixels that have a flux tower without any knowledge of the spatial extent and relative importance of upwind source areas (footprint). Because all of these sites except for the Charleston Mesquite site are part of FLUXNET [43], we have included additional details and discussion on the Charleston Mesquite site. The data used from the FLUXNET sites are Level 2 data, so they have data gaps ranging from about 7% (Flagstaff wildfire site) to 22% (Santa Rita Creosote site). The data collection and methodology for FLUXNET sites were according to Ameriflux protocol described in the references given in Table 2. The Charleston Mesquite site is located at an elevation of 1200 m, about 16 km northeast of Sierra Vista, Arizona, on the east side of the San Pedro River. This site is dense riparian woodland dominated by velvet mesquite (*Prosopis velutina*), while the understory is composed of sacaton grass (*Sporobolus wrightii*), greythorn shrubs (*Zizyphus obtusifolia*), and other summer active annual herbaceous species. The average canopy cover is about 70% with leaf area index ranging from about 1.2 prior to leaf-out to about 2 during most of the growing season. A three-dimensional sonic anemometer (Model CSAT3, Campbell Scientific Inc., Logan, UT, USA) and an open path infrared gas analyzer (IRGA; Model LI-7500, LI-COR Inc., Lincoln, NE, USA) were used at the site. The variables were sampled at 10 Hz by a datalogger (CR5000, Campbell Scientific Inc., Logan, UT, USA) and averaged over 30-min. The average depth to groundwater was about 10 m. Other details of the Charleston Mesquite site and measurement techniques are described elsewhere [42,44].

Table 2. Details of eddy covariance tower validation sites used in this study.

Sl. No.	Site Name	Code	Latitude (Degree)	Longitude (degree)	Elevation (m)	Tower Height (m)	Land Cover	Landsat Path/Row	No. of Cloud-Free Images	Reference
1	Flagstaff managed forest	FMF	35.1426	−111.7273	2160	23	Ponderosa pine forest	37/36	6	Dore <i>et al.</i> (2012) [38]
2	Flagstaff unmanaged forest	FUF	35.089	−111.762	2180	23	Ponderosa pine forest	37/36	6	Dore <i>et al.</i> (2012) [38]
3	Flagstaff wildfire	FWF	35.4454	−111.7718	2270	4	Ponderosa pine forest	37/35	7	Dore <i>et al.</i> (2012) [38]

Table 2. Cont.

Sl. No.	Site name	Code	Latitude (Degree)	Longitude (degree)	Elevation (m)	Tower Height (m)	Land Cover	Landsat Path/Row	No. of Cloud-Free Images	Reference
4	Santa Rita Creosote	SRC	31.9083	−110.8395	991	4.25	Open shrub land	36/38	9	Kure and Benton (2010) [39]
5	Santa Rita Mesquite	SRM	31.8214	−110.8661	1120	6.4	Woody Savannas	36/38	9	Scott <i>et al.</i> (2009) [40]
6	Kendall Grassland	WKG	31.7365	−109.9419	1531	6.4	Grassland	35/38	7	Scott <i>et al.</i> (2010) [41]
7	Charleston Mesquite	CMS	31.6637	−110.1776	1200	14	Riparian woodland	35/38	7	Scott <i>et al.</i> (2004) [42]

3. Results and Discussion

3.1. Annual ET_a of Different Land Use/Land Cover

Spatial distribution of the first ever annual ET_a of the CRB at the Landsat scale showed different water use patterns within the basin (Figure 4). As expected, open water had the highest mean annual water loss (994 mm) followed by cropland (538 mm) as a result of evapotranspiration (Table 3). There was a wide spatial variation (high standard deviation) in annual ET_a of different land cover classes (Table 3). The standard deviation of mean annual ET_a ranged from 144 mm (grassland) to 699 mm (water). A wide range of mean annual ET_a may be attributed to many variables including thematic accuracy of the NLCD 2006 map, changes in land use from 2006 to 2010, topography, cropping system, cropping intensity, irrigation, local climatic conditions, and Landsat scene availability for ET_a mapping. In general, thematic accuracy of the Level II NLCD map is less than 80% [45]. This means many land cover classes may be misclassified, resulting in a wide range of annual ET_a . However, the classification errors aggregated over a larger area do not result in significant error [46]. Cultivation of different crops will also result in a wide variation of actual ET as different crops have different water requirements based on plant physiology and crop duration. Similarly, growing more than one crop per year will result in higher ET_a than growing only one crop per year. There will also be a difference in ET_a of the same crop under irrigated and non-irrigated conditions because irrigation leads to increased ET_a . A study on the effect of irrigation on the water and energy balance of the CRB has shown decreased stream flow and surface temperature [47]. The climatic gradient within the basin due to its large size and relief will also cause differences in the water use pattern.

As an example, the histogram of annual ET_a for some of the land cover classes for path 37/row 37 (Figure 3) is presented in Figure 5. A majority (76%) of the barren land pixels had an annual ET_a within 100–200 mm, and very few pixels (4%) had an annual ET_a greater than 500 mm. Similarly, about half of the grassland (47%) had an annual ET_a between 200 and 300 mm and less than 5% exceeded 500 mm. In contrast, annual ET_a was greater than 800 mm in the majority of cropland. Some of the cropland was fallow based on visual interpretation during 2010 resulting in an annual ET_a similar to grassland and barren land. In addition, the effect of misclassification in NLCD 2006 and/or

change of land cover may be attributed to low annual ET_a of cropland and high annual ET_a of barren land and grassland.

Westenburg *et al.* (2006) [48] collected ET_a data from three sites in Havasu National Wildlife Refuge during 2002–2004 using Bowen ratio stations. These sites included a large area of medium-to-high density, homogeneous saltcedar (*Tamarix spp.*); an area of medium density mixed vegetation; and a homogeneous area of low-to-medium density arrowweed. They reported annual ET_a for 2003 for saltcedar, mixed vegetation, and arrowweed as 1,076 mm, 728 mm, and 716 mm, respectively. Our results for these sites showed annual ET_a for 2010 as 1,291 mm, 1,089 mm, and 1,333 mm, respectively. It appears that ET_a increased during these 7 years particularly for mixed vegetation and arrowweed. Doody *et al.* (2011) [49] listed ET_a of some of the cover types based on reviewed literatures. They reported annual ET_a of arrowweed as 1,370–1,590 mm, very close to our result for arrowweed. They found a wide range of annual ET_a for saltcedar, ranging from 220 to 1,460 mm with a mean value of 765 ± 413 mm. They reported annual ET_a for bare soil as 307 mm and for open water as 1,156 mm. Thus, overall our results for these locations and cover types are similar and comparable.

Figure 4. Spatial distribution of evapotranspiration in the Colorado River Basin for 2010 using Landsat images.

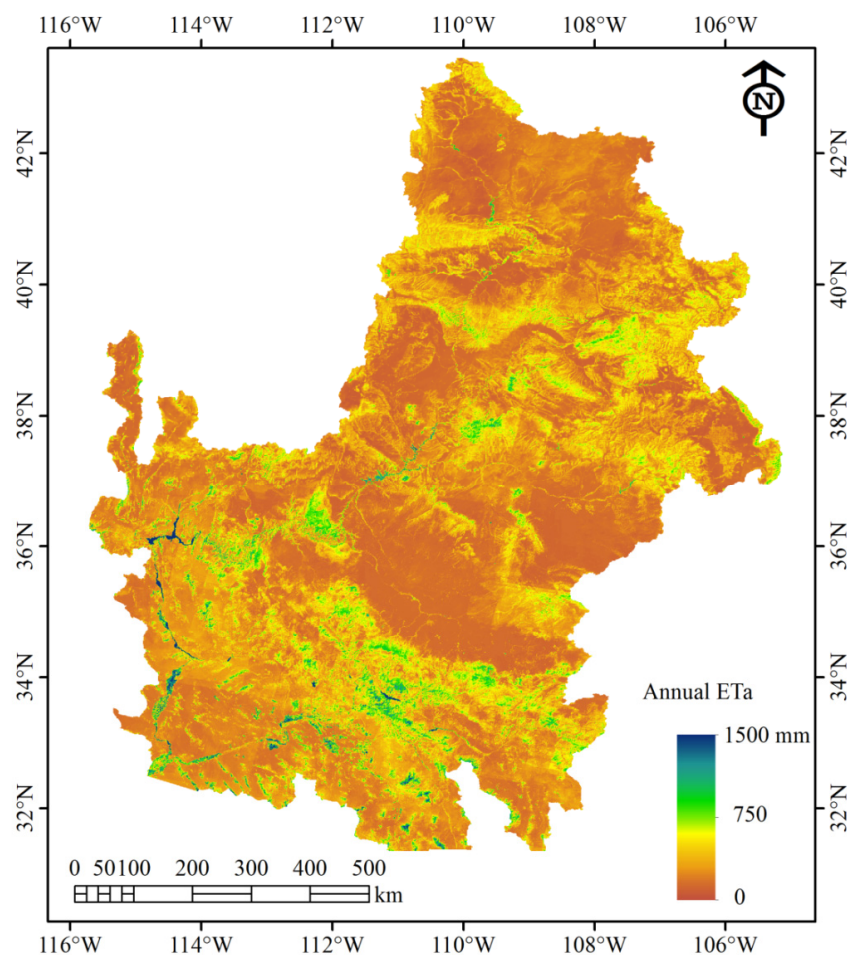
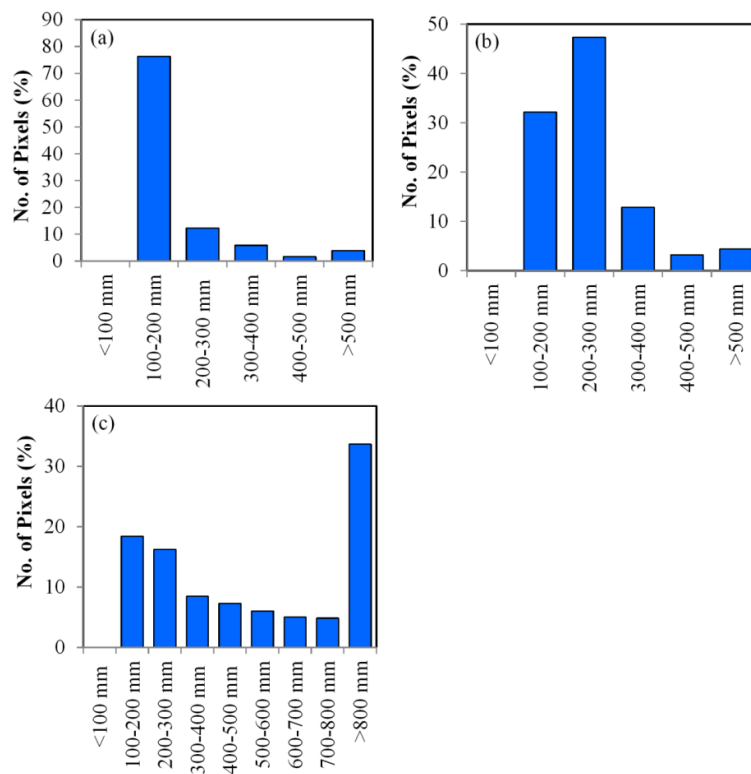


Table 3. Annual evapotranspiration (mm) during 2010 for different National Land Cover Database [24] land use/land cover within the study area.

Land Use/Land cover	Mean Annual ET _a (mm)	Standard Deviation (mm)
Water	994	699
Ice/snow	405	168
Open space development	323	227
Low intensity development	374	245
Med. intensity development	397	213
High intensity development	386	222
Barren land	283	198
Deciduous forest	434	189
Evergreen forest	447	223
Mixed forest	515	186
Shrubland	262	182
Grassland	224	144
Pasture/Hay	365	271
Cropland	538	393
Woody Wetland	421	301
Herb. Wetland	337	283

Figure 5. Histogram of the annual evapotranspiration for selected land cover classes (a) Barren land; (b) Grassland; and (c) Cropland within the Landsat path 37/row37.



Nagler *et al.* (2005) [50] calculated spatial ET for the Lower Colorado River stretch at Havasu National Wildlife Refuge based on MODIS-enhanced vegetation index and air temperature. They

found that the annual ET_a of the area during 2000–2003 ranged from 832 mm (2000) to 881 mm (2002) with a mean ET_a of 851 mm. Our zonal analysis of the same region showed mean annual ET_a of 865 mm. Though we did not use exactly the same areal extent because our delineation slightly differed from theirs, the comparable mean ET_a shows that our results are reliable. Even though there is a wide range in the standard deviation of different land cover classes, the mean annual ET_a values are comparable to some of the measured and reported ET_a in the CRB.

3.2. Validation with Eddy Covariance Measurement

Figure 6 shows the comparison of annual ET_a measured by eddy covariance against Landsat annual ET_a for all seven validation sites within the study area. Overall, the SSEBop-estimated ET_a was in good agreement ($R^2 = 0.78$) with the measured ET_a for a wide range of elevations (991–2,270 m) and tower heights (4–23 m) (Table 2). The mean difference between measured and estimated annual ET_a was about 10%, which is comparable with results from other energy balance based models [5,17]. The root mean square error (RMSE) was 106 mm, mainly due to the high discrepancy at the Flagstaff unmanaged forest and Flagstaff wildfire sites (Figure 6). If these two sites are removed, then R^2 improves to 0.95 ($Y = 0.997 X - 53.767$) and RMSE decreases to 68 mm. This is remarkable considering we had only 6–9 cloud-free Landsat scenes for 2010 (Table 2) and we had not carried out any calibration of our model using eddy covariance measurements.

Figure 6. Validation of Landsat-based annual evapotranspiration with eddy covariance measured evapotranspiration at Flagstaff managed forest (FMF), Flagstaff unmanaged forest (FUF), Flagstaff wildfire (FWF), Santa Rita Creosote (SRC), Santa Rita Mesquite (SRM), Kendall Grassland (WKG), and Charleston Mesquite (CMS) sites. Removal of FUF and FWF sites resulted in $y = 0.997x - 53.767$ ($R^2 = 0.95$) and RMSE of 68 mm.

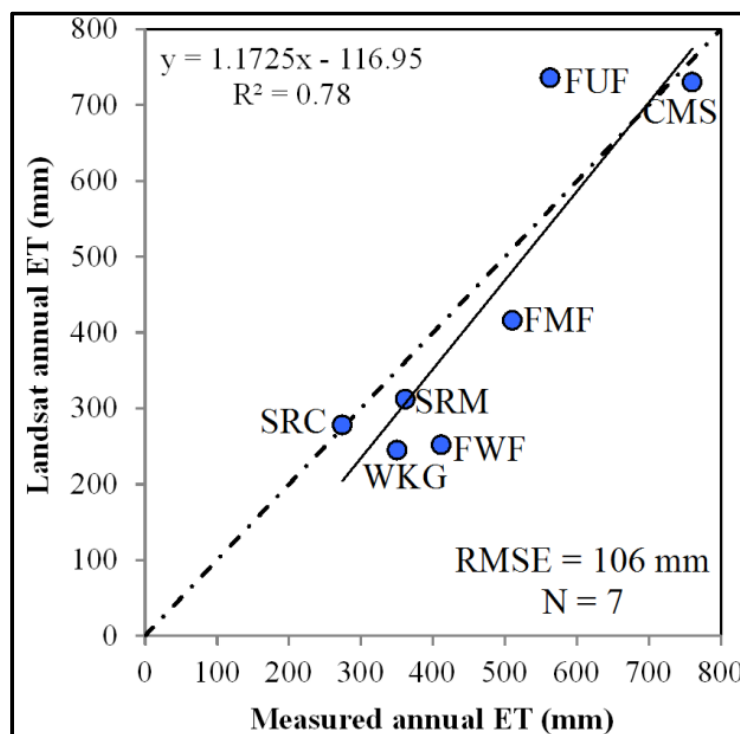


Figure 7. Annual evapotranspiration values for 5×5 Landsat pixels centered over the eddy covariance tower at the Flagstaff managed forest (FMF), Flagstaff unmanaged forest (FUF), Flagstaff wildfire (FWF), Santa Rita Creosote (SRC), Santa Rita Mesquite (SRM), Kendall Grassland (WKG), and Charleston Mesquite (CMS) sites.

404	446	488	470	470
462	436	428	421	415
448	423	416	415	422
409	408	391	404	411
386	391	392	385	391
FMF				
738	726	719	712	691
699	725	725	726	738
717	734	736	734	734
669	686	720	713	703
693	669	696	698	731
FUF				
232	269	259	223	166
235	256	256	256	255
252	262	252	249	249
245	251	242	242	245
248	248	239	239	239
FWF				
286	314	310	313	313
309	304	305	276	276
303	278	278	279	270
279	289	289	294	287
312	307	307	305	296
SRC				
331	332	331	332	318
317	321	321	312	312
301	321	312	312	312
270	289	302	306	306
279	283	306	297	302
SRM				
231	234	255	241	205
224	220	245	212	186
224	220	245	212	186
213	214	219	192	202
183	214	253	231	202
WKG				
681	686	691	709	718
693	698	700	706	706
716	715	730	732	722
715	739	750	757	730
710	731	742	752	711
CMS				

It should be noted that we have compared the measured ET_a only with the ET of the pixel that has a flux tower. However, the point distribution in Figure 6 shows that the SSEBop model captured the ET variability well even without footprint analysis. In general, the footprint of a point of observation is affected by thermal stability, surface roughness, observation levels, and wind speed and direction [51]. Since the wind direction is variable throughout the year, an exact footprint analysis is simply impossible to carryout [52]. The advantage of having a remote sensing based ET map is that we get spatial and

temporal distribution of ET, thus not requiring any footprint analysis. For example, Figure 7 shows the ET values for 5×5 Landsat pixels centered over the eddy covariance tower. We can see there is variability in ET values even within $150 \text{ m} \times 150 \text{ m}$ (5×5 pixels), an area smaller than a generally used 100-to-1 fetch-to height ratio for sites (considering the tower height given in Table 2). Based on measured ET values, we can get a good sense of footprint direction and our results are in reasonable agreement. For example, wind direction at the Flagstaff unmanaged forest site was mostly from the southwest, where pixels had lower ET_a values (Figure 7).

Though we have not carried out uncertainty analysis in the present study, like any other models, our model result may have some uncertainty. There are also systematic and random errors associated with the eddy covariance measurements [53–55]. The total annual precipitation and ET_a measured at the Charleston Mesquite site during 2010 were 266 mm and 673 mm, respectively. Our SSEBop model-estimated ET_a at the site was 730 mm, which is only about 8% higher than the measured value. At this site, there is a lack of energy balance closure by about 11% (on a daily basis) in the eddy covariance measurements, and this is generally the case at most eddy covariance sites. Wilson *et al.* (2002) [54] evaluated eddy covariance measurements across 22 FLUXNET sites (50 site-years) and reported that the mean imbalance between turbulent energy fluxes (sensible and latent heat fluxes) and available energy (net radiation minus soil heat flux) is on the order of 20%. For forced energy balance closure we scaled the latent and sensible heat fluxes conserving the measured Bowen ratio. The scaled up ET_a for energy balance closure at the site was 761 mm. Thus, there was only 4% difference between the scaled up measured ET_a and the modeled ET_a , giving us good confidence in the annual value at the pixel level. Our result is within the range of general ET_a estimation accuracy reported for seasonal ET_a using remote sensing models.

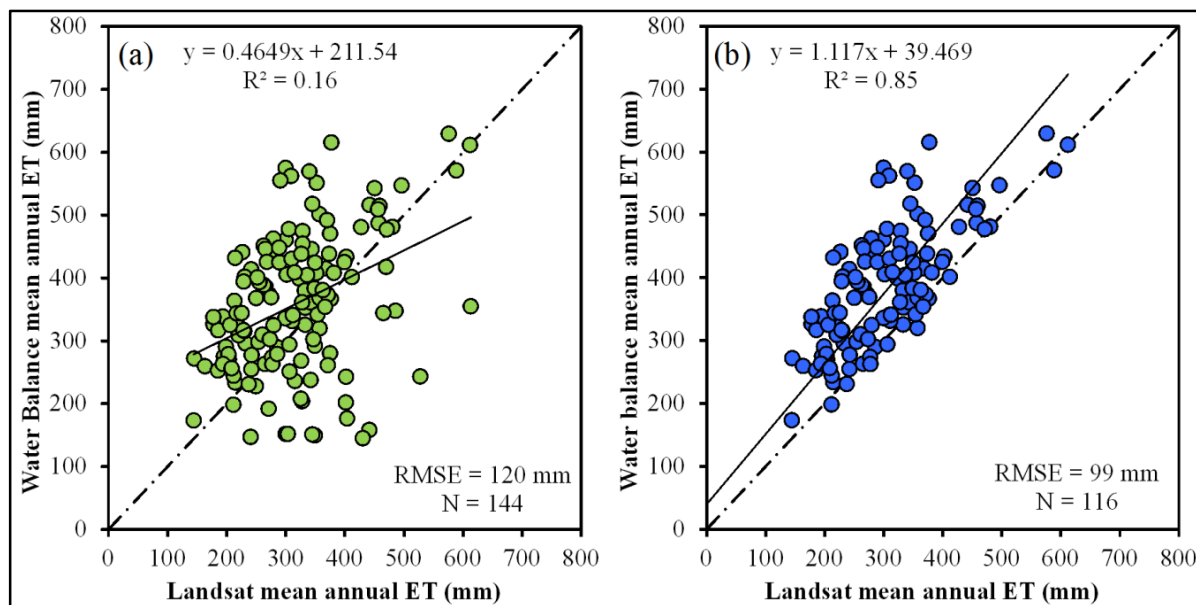
Jung *et al.* (2009) [35] used eddy covariance data from FLUXNET and developed a global, spatially and temporally explicit ET_a map (gridded flux data) using model tree ensemble, a machine learning technique. We used this gridded flux data (written communication 2013) to compare our result. The mean annual ET_a of the CRB for 2010 using gridded flux data was 292 mm. Our result showed that the mean annual ET_a of the CRB is 312 mm. These values are comparable (within 7%) in spite of very coarse (50 km) spatial resolution of gridded flux data against this high resolution (30 m) Landsat data.

3.3. Comparison with Annual ET_a Based on Water Balance Analysis

The Landsat-based mean annual ET_a of HUC8 ranged from 144 mm (Upper Green-Slate in Upper Colorado basin) to 613 mm (Lower Salt in Lower Colorado basin), while mean annual ET_a based on water balance ranged from 145 mm (Yuma desert in Lower Colorado basin) to 629 mm (Tonto sub-basin in Lower Colorado basin). Comparison of Landsat-based mean annual ET_a with that of water balance-based mean annual ET_a at the HUC8 level has shown that some HUC8 had very good correspondence while other HUC8 were scattered (Figure 8). This finding is expected as ET_a based on water balance assumes mass balance closure at the annual scale. In reality, basin runoff exhibits strong memory from year to year and water balance may not close even over a year due to time lag. Overall, there was poor correlation ($R^2 = 0.16$) between annual ET_a based on Landsat and annual ET_a based on water balance. Most of the mismatch between Landsat and water balance-based ET_a is in sub-basins having large irrigated cropland or water bodies or where vegetation has access to groundwater thus

invalidating the premise of water balance closure. We used three sub-criteria to remove some HUC8 sub-basins where water balance may not close because (1) mean runoff is more than mean precipitation, *i.e.*, sub-basins where base flow is dominant; (2) mean ET_a is more than mean precipitation, *i.e.*, sub-basins where mostly irrigated or open water bodies are dominant; and (3) the runoff ratio (Q/P) is greater than 0.55, indicating large seepage loss/base flow/percolation loss. Out of 144 sub-basins within the CRB, 28 sub-basins were removed from the analysis based on these three criteria. This resulted in significant improvement of R^2 from 0.16 to 0.85, and RMSE decreased from 120 mm to 99 mm. The regression line shows that annual ET_a based on water balance was about 12% higher than Landsat-based ET_a . This is reasonable considering that water balance-based ET_a is computed neglecting the storage term in the water balance equation thus overestimating annual ET_a . In general, the accuracy of ET_a products at a higher HUC level (HUC8) is lower than the accuracy at a lower HUC level (HUC2) [56]. Our results show that even at the HUC8 level, Landsat-based ET_a explained about 85% variability in ET_a based on water balance. Compared to mean annual ET_a , there was wide range in areal extent of sub-basins within the CRB, ranging from 381 km² (Cloverdale in Lower Colorado basin) to 11,845 km² (Chaco in Upper Colorado basin). A sub-basin having smaller mean ET_a but larger area can have larger volume of water lost due to ET_a . Thus, spatial distribution of ET_a based on remotely sensed data at the sub-basin level can help water managers identify the water surplus and water deficit sub-basins and quantify the water availability.

Figure 8. Comparison of mean annual evapotranspiration based on water balance (Precipitation–runoff) and Landsat-based mean annual evapotranspiration for (a) all HUC8 sub-basins; and (b) HUC8 sub-basins meeting three criteria: precipitation > runoff, Evapotranspiration < precipitation, and runoff coefficient (Q/P) < 0.55.



3.4. Comparison with MODIS-Based Annual ET_a

We also compared our Landsat-estimated ET with that obtained from MODIS-based annual ET. Senay *et al.* (2013) [16] used the SSEBop model with the MODIS images for 2005, and their monthly

ET validation with 45 Ameriflux data sites for the conterminous United States resulted in an R^2 of 0.64 with RMSE of 27 mm. With more years (2000–2007), MODIS-based annual ET_a using the SSEBop model has resulted in a high skill score across all the climate zones in the western United States [56]. Spatial distribution of annual ET_a using 2010 MODIS images has shown consumptive water use distribution within the CRB (Figure 9). In general, we can see that the ET_a distribution pattern using MODIS and Landsat images is similar. Our comparison of Landsat-based annual ET_a and MODIS-based annual ET_a for all 144 HUCs (level 8) showed that there was good agreement (Figure 10). The coefficient of determination ($R^2 = 0.79$) indicated that we can obtain a comparable ET_a estimate even with the coarse resolution (1 km) of MODIS at the sub-basin (HUC8) level. However, the advantages of Landsat-based annual ET_a become obvious when ET_a is required at fine resolution (field scale). Figure 11 shows the annual ET_a distribution in a small part of Colorado using Landsat and MODIS images. The ET_a variation within individual center-pivot irrigation fields is clearly visible in the Landsat-based ET_a estimate, but there is no distinction between fields in the MODIS-based ET_a estimates. This is of high importance particularly for implementing water management decisions at the local level. For example, water conservation measures can be adopted in the fields that have higher ET_a than surrounding fields. Besides improving efficiency, this can save energy and water that can be used elsewhere. As tackling water challenges is one of the highest priority initiatives under the DOI WaterSMART Program, ET_a estimates at the field scale will help in water conservation, availability, and water conflict resolution.

Figure 9. Spatial distribution of evapotranspiration in the Colorado River Basin for 2010 using MODIS images.

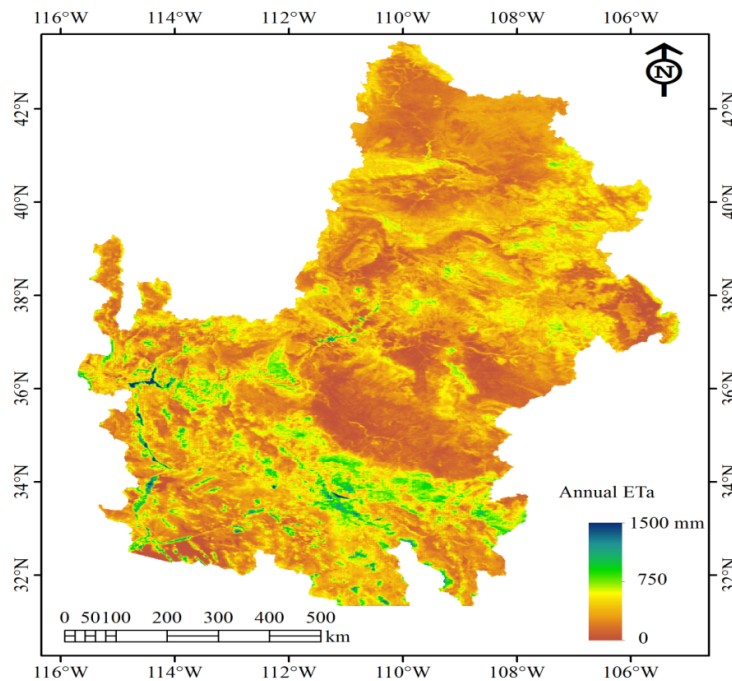


Figure 10. Comparison of mean annual evapotranspiration of sub-basins (HUC8) using Landsat and MODIS images.

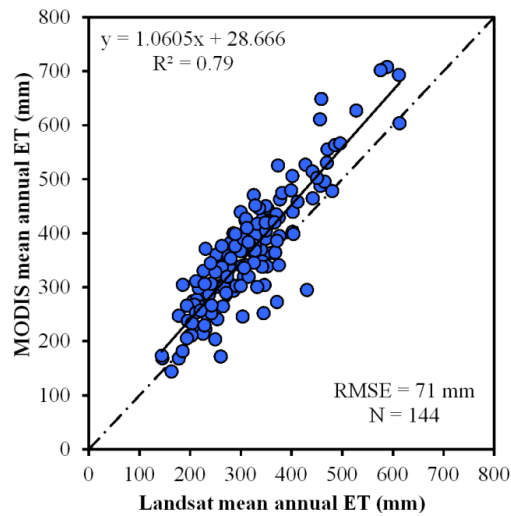
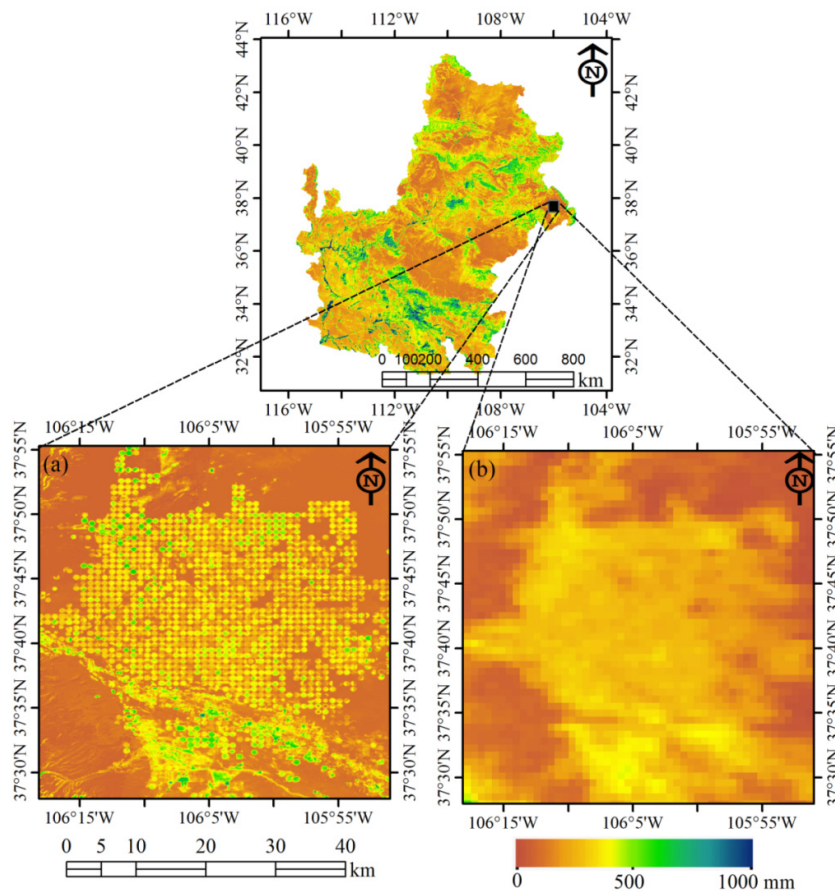


Figure 11. Example showing the spatial distribution of annual evapotranspiration map of the same area within the Colorado River Basin with (a) zoomed in view of the Landsat-based evapotranspiration map for the area in the black square; and (b) zoomed in view of the MODIS-based evapotranspiration map in the black square area. Legend and scale shown at the bottom are for images Figure 11a,b.



As modelers, we recognize that model development is a continuous process. As with any other models, our model has continued evolving since its first publication [14]. With the availability of better data sources, our model output will also improve as a result of using better input data. For example, the use of Daymet (Thornton *et al.*, 1997) [57], daily climatological data is expected to give better results than monthly PRISM air temperature data. Similarly, North American Land Data Assimilation System (NLDAS) (Mitchell *et al.*, 2004) [58], which is a quality-controlled and spatially and temporally consistent land surface model dataset (1/8th degree spatial resolution), may improve ET_o and thus ET_a estimates.

4. Conclusions

Accurate information on water availability and water use is necessary for planning sustainable use of water, particularly in an arid region like the southwestern United States. Though detailed information on water availability in the Colorado River Basin is available, there is a need for reliable estimation of spatially distributed water use. We have developed a basin-wide ET_a map of the Colorado River Basin using images from Landsat, the longest existing polar orbiting satellite. The first ever ET_a map of the Colorado River Basin at Landsat scale has shown the distribution pattern of ET_a , which is based on the scientifically robust and operationally viable SSEBop model. We have demonstrated that, in spite of the complexities of the CRB, seamless ET_a based on remote sensing can be estimated at the Landsat scale. Though cropland covers less than 1% of the CRB, it has the highest ET_a after open water bodies. There was a wide variation in ET_a within most land use/land cover classes in the basin due to hydro-climatic variation within the basin and uncertainty in the land cover classification. Validation of Landsat-based estimated ET_a with ET_a measured using eddy covariance has shown that there was good correspondence ($R^2 = 0.78$) and the model captured the variability of ET_a over a wide range of elevation and tower height. The R^2 improved to 0.95 with a slope of 0.997 when two sites (FUF and FWF) were removed from validation. The SSEBop model-estimated ET_a was within 4% of the measured ET_a at two sites (SRC and CMS). Comparison with ET_a based on water balance at the HUC8 level showed good agreement ($R^2 = 0.85$) for sub-basins most likely having water balance closure. ET_a maps using Landsat and MODIS images showed a similar water use pattern at the regional scale. However, the advantages of the Landsat images were clearly observed when the ET_a map was zoomed in for field-level ET_a distribution. In contrast with MODIS-based ET_a maps, individual fields are clearly distinguishable in Landsat-based ET_a maps. Thus, Landsat-based ET_a mapping is better suited for planning and management of water resources at the field scale.

ET_a based on remote sensing may have biases, but these biases can be easily identified and removed based on validation using reliable field data. Once the bias is removed, consistent ET_a maps can be generated for regular ET_a mapping and water resources planning and management. A regular production of Landsat-based ET_a maps using a uniform method and data source at a seasonal and annual scale has the potential for resolving inconsistencies arising from using different methods and variable data sources. With further validation using multiple years and sites, our methodology can be applied for larger areas such as the conterminous United States.

Acknowledgments

This work was performed under U.S. Geological Survey (USGS) contract G23PC00028 and G10PC00044 in support of the WaterSMART program. We acknowledge with thanks the internal review of the manuscript by Roger Auch, USGS Earth Resources Observation and Science Center. We gratefully acknowledge the use of Ameriflux data for our model validation. We are thankful to the four anonymous reviewers for their thoughtful comments and helpful suggestions on an earlier version of the manuscript. Any use of trade, firm, or product names is for descriptive purposes only and does not imply endorsement by the US Government.

Conflicts of Interest

The authors declare no conflict of interest.

References

1. Christensen, N.S.; Wood, A.W.; Voisin, N.; Lettenmaier, D.P.; Palmer, R.N. The effects of climate change on the hydrology and water resources of the Colorado River Basin. *Clim. Chang.* **2004**, *62*, 337–363.
2. McCabe, G.J.; Wolock, D.M. Warming may create substantial water supply shortages in the Colorado River Basin. *Geophys. Res. Lett.* **2007**, *34*, L22708.
3. Bastiaanssen, W.G.M.; Molden, D.J.; Makin, I.W. Remote sensing for irrigated agriculture: Examples from research and possible applications. *Agric. Water Manag.* **2000**, *46*, 137–155.
4. Nagler, P.L.; Glenn, E.P.; Didan, K.; Osterberg, J.; Jordan, F.; Cunningham, J. Wide-area estimates of stand structure and water use of *Tamarix spp.* on the Lower Colorado River: Implications for restoration and water management projects. *Restor. Ecol.* **2008**, *16*, 136–145.
5. Gowda, P.H.; Chavez, J.L.; Colaizzi, P.D.; Evett, S.R.; Howell, T.A.; Tolk, J.A. ET Mapping for agricultural water management: Present status and challenges. *Irrig. Sci.* **2008**, *26*, 223–237.
6. Menenti, M.; Chaudhury, B.J. Parameterization of Land Surface Evapotranspiration Using a Location Dependent Potential Evapotranspiration and Surface Temperature Range. In Proceedings of the Exchange Processes at the Land Surface for a Range of Space and Time Scales; Bolle, H.J., Feddes, R.A., Kalma, J.D., Eds.; International Association of Hydrological Sciences: Rennes, France, 1993; Volume 212, pp. 561–568.
7. Norman, J.M.; Kustas, W.P.; Humes, K.S. A two-source approach for estimating soil and vegetation energy fluxes from observations of directional radiometric surface temperature. *Agric. For. Meteorol.* **1995**, *77*, 263–293.
8. Bastiaanssen, W.G.M.; Menenti, M.; Feddes, R.A.; Holtslag, A.A.M. The surface energy balance algorithm for land (SEBAL): Part 1 Formulation. *J. Hydrol.* **1998**, *212–213*, 198–212.
9. Roerink, G.J.; Su, Z.; Menenti, M. S-SEBI: A simple remote sensing algorithm to estimate the surface energy balance. *Phys. Chem. Earth Part B* **2000**, *25*, 147–157.
10. Su, Z. The Surface Energy Balance System (SEBS) for estimation of turbulent heat fluxes. *Hydrol. Earth Syst. Sci.* **2002**, *6*, 85–99.

11. Loheide, S.P., II; Gorelick, S.M. A local-scale, high resolution evapotranspiration mapping algorithm (ETMA) with hydroecological applications at riparian meadow restoration sites. *Remote Sens. Environ.* **2005**, *98*, 182–200.
12. Anderson, M.C.; Norman, J.M.; Mecikalski, J.R.; Otkin, J.A.; Kustas, W.P. A Climatological study of evapotranspiration and moisture stress across the continental United States based on thermal remote sensing: 1 Model formulation. *J. Geophys. Res.* **2007**, doi: 10.1029/2006JD007506.
13. Allen, R.G.; Tasumi, M.; Trezza, R. Satellite-based energy balance for mapping evapotranspiration with internalized calibration (METRIC)—Model. *ASCE J. Irrig. Drain. Eng.* **2007**, *133*, 380–394.
14. Senay, G.B.; Budde, M.E.; Verdin, J.P.; Melesse, A.M. A coupled remote sensing and Simplified Surface Energy Balance (SSEB) approach to estimate actual evapotranspiration from irrigated fields. *Sensors* **2007**, *7*, 979–1000.
15. Singh, R.K.; Irmak, A. Treatment of anchor pixels in the METRIC model for improved estimation of sensible and latent heat fluxes. *Hydrol. Sci. J.* **2011**, *56*, 895–906.
16. Senay, G.B.; Bohms, S.; Singh, R.K.; Gowda, P.H.; Velpuri, N.M.; Alemu, H.; Verdin, J.P. Operational evapotranspiration mapping using remote sensing and weather datasets: A new parameterization for the SSEB approach. *J. Am. Water Resour. Assoc.* **2013**, *49*, 577–591.
17. Gowda, P.H.; Chavez, J.L.; Colaizzi, P.D.; Evett, S.R.; Howell, T.A.; Tolk, J.A. Remote sensing based energy balance algorithms for mapping ET: Current status and future challenges. *Trans. Am. Soc. Agric. Biol. Eng.* **2007**, *50*, 1639–1644.
18. Kalma, J.D.; McVicar, T.R.; McCabe, M.F. Estimating land surface evaporation: A review of methods using remotely sensed surface temperature data. *Surv. Geophys.* **2008**, *29*, 421–469.
19. Glenn, E.P.; Neale, C.M.U.; Hunsaker, D.J.; Nagler, P.L. Vegetation index-based crop coefficients to estimate evapotranspiration by remote sensing in agricultural and natural ecosystems. *Hydrol. Process.* **2011**, *25*, 4050–4062.
20. US Geological Survey (USGS). Facing Tomorrow's Challenges—U.S. Geological Survey Science in the Decade 2007–2017. *US Geol. Surv. Circ.* **2007**, *1309*, 1–69.
21. US Department of the Interior (DOI). Fiscal Year 2011 The Interior Budget in Brief. In *WaterSMART: Departmental Highlights*; US Department of the Interior: Washington DC, USA, 2010; pp. 19–25.
22. Bruce, B.W. *WaterSMART—The Colorado River Basin Focus Area Study*; US Geological Survey: Washington DC, USA.
23. Allen, R.G.; Pereira, L.S.; Raes, D.; Smith, M. *Crop Evapotranspiration: Guidelines for Computing Crop Water Requirements*; FAO: Rome, Italy, 1998.
24. Fry, J.; Xian, G.; Jin, S.; Dewitz, J.; Homer, C.; Yang, L.; Barnes, C.; Herold, N.; Wickham, J. Completion of the 2006 national land cover database for the conterminous United States. *Photogramm. Eng. Remote Sens.* **2011**, *77*, 858–864.
25. Bureau of Reclamation (BOR). *Lower Colorado River Accounting System, Demonstration of Technology*; Lower Colorado Regional Office: Boulder City, NV, 1997.
26. Congalton, R.G.; Balogh, M.; Bell, C.; Green, K.; Milliken, J.A.; Ottman, R. Mapping and monitoring agricultural crops and other land cover in the Lower Colorado River Basin. *Photogramm. Eng. Remote Sens.* **1998**, *64*, 1107–1114.

27. Kumar, M.; Duffy, C.J. Detecting hydroclimatic change using spatio-temporal analysis of time series in Colorado River Basin. *J. Hydrol.* **2009**, *374*, 1–15.
28. Chander, G.; Markham, B.L.; Helder, D.L. Summary of current radiometric calibration coefficients for Landsat MSS, TM, ETM+, and EO-1 ALI sensors. *Remote Sens. Environ.* **2009**, *113*, 893–903.
29. Tasumi, M.; Allen, R.; Trezza, R. At-surface reflectance and albedo from satellite for operational calculation of land surface energy balance. *J. Hydrol. Eng.* **2008**, *13*, 51–63.
30. Daly, C.; Gibson, W.P.; Taylor, G.H.; Johnson, G.L.; Pasteris, P. A knowledge-based approach to the statistical mapping of climate. *Clim. Res.* **2002**, *22*, 99–113.
31. US Geological Survey (USGS). Waterwatch—Maps, Graphs, and Tables of Current, Recent, and Past Streamflow Conditions. Available online: <http://pubs.usgs.gov/fs/2008/3031/> (accessed on 31 December 2012).
32. Reuter, H.I.; Nelson, A.; Jarvis, A. An evaluation of void filling interpolation methods for SRTM data. *Int. J. Geogr. Inf. Sci.* **2007**, *21*, 983–1008.
33. Senay, G.B.; Verdin, J.P.; Lietzow, R.; Melesse, A.M. Global reference evapotranspiration modeling and evaluation. *J. Am. Water Resour. Assoc.* **2008**, *44*, 969–979.
34. Kanamitsu, M. Description of the NMC global data assimilation and forecast system. *Weather Forecast.* **1989**, *4*, 335–342.
35. Jung, M.; Reichstein, M.; Bondeau, A. Towards global empirical upscaling of FLUXNET eddy covariance observations: Validation of a model tree ensemble approach using a biosphere model. *Biogeosciences* **2009**, *6*, 2001–2013.
36. Singh, R.K. Geospatial Approach for Estimating Land Surface Evapotranspiration. Ph.D. Dissertation, University of Nebraska-Lincoln, Lincoln, NE, USA, 2009.
37. Singh, R.K.; Liu, S.; Tieszen, L.L.; Suyker, A.E.; Verma, S.B. Estimating seasonal evapotranspiration from temporal satellite images. *Irrig. Sci.* **2012**, *30*, 303–313.
38. Dore, S.; Montes-Helu, M.; Hart, S.C.; Hungate, B.A.; Koch, G.W.; Moon, J.B.; Finkral, A.J.; Kolb, T.E. Recovery of ponderosa pine ecosystem carbon and water fluxes from thinning and stand-replacing fire. *Glob. Chang. Biol.* **2012**, *18*, 3171–3185.
39. Kurc, S.A.; Benton, L.M. Digital image-derived greenness links deep soil moisture to carbon uptake in a creosotebush-dominated shrubland. *J. Arid Environ.* **2010**, *74*, 585–594.
40. Scott, R.L.; Jenerette, G.D.; Potts, D.L.; Huxman, T.E. Effects of seasonal drought on net carbon dioxide exchange from a woody-plant-encroached semiarid grassland. *J. Geophys. Res.: Biogeosci.* **2009**, *114*, G04004.
41. Scott, R.L.; Hamerlynck, E.P.; Jenerette, G.D.; Moran, M.S.; Barron-Gafford, G. Carbon dioxide exchange in a semidesert grassland through drought-induced vegetation change. *J. Geophys. Res.: Biogeosci.* **2010**, doi: 10.1029/2010JG001348.
42. Scott, R.L.; Edwards, E.A.; Shuttleworth, W.J.; Huxman, T.E.; Watts, C.; Goodrich, D.C. Interannual and seasonal variation in fluxes of water and carbon dioxide from a riparian woodland ecosystem. *Agric. For. Meteorol.* **2004**, *122*, 65–84.

43. Baldocchi, D.; Falge, E.; Gu, L.; Olson, R.; Hollinger, D.; Running, S.; Anthoni, P.; Bernhofer, C.; Davis, K.; Evans, R.; *et al.* FLUXNET: A new tool to study the temporal and spatial variability of ecosystem-scale carbon dioxide, water vapor, and energy flux densities. *Bull. Am. Meteorol. Soc.* **2001**, *82*, 2415–2431.
44. Barron-Gafford, G.A.; Scott, R.L.; Jenerette, G.D.; Hamerlynck, E.P.; Huxman, T.E. Temperature and precipitation controls over leaf and ecosystem-level CO₂ flux along a woody plant encroachment gradient. *Glob. Chang. Biol.* **2012**, *18*, 1389–1400.
45. Wickham, J.D.; Stehman, S.V.; Gass, L.; Dewitz, J.; Fry, J.A.; Wade, T.G. Accuracy assessment of NLCD 2006 land cover and impervious surface. *Remote Sens. Environ.* **2013**, *130*, 294–304.
46. Stehman, S.V.; Milliken, J.A. Estimating the effect of crop classification error on evapotranspiration derived from remote sensing in the Lower Colorado River basin, USA. *Remote Sens. Environ.* **2007**, *106*, 217–227.
47. Haddeland, I.; Lettenmaier, D.P.; Skaugen, T. Effects of irrigation on the water and energy balances of the Colorado and Mekong River basins. *J. Hydrol.* **2006**, *324*, 210–223.
48. Westenburg, C.L.; Harper, D.P.; DeMeo, G.A. Evapotranspiration by Phreatophytes along the Lower Colorado River at Havasu National Wildlife Refuge, Arizona; US Geological Survey Scientific Investigations Report 2006–5043; US Department of the Interior: Washington DC, USA, 2006; p. 44.
49. Doody, T.M.; Nagler, P.M.; Glenn, E.P.; Moore, G.W.; Morino, K.; Hultine, K.R.; Benyon, R.G. Potential for water salvage by removal of non-native woody vegetation from dryland river systems. *Hydrol. Process.* **2011**, *25*, 4117–4131.
50. Nagler, P.L.; Scott, R.L.; Westenburg, C.; Cleverly, J.R.; Glenn, E.P.; Huete, A.R. Evapotranspiration on western US rivers estimated using the enhanced vegetation index from MODIS and data from eddy covariance and Bowen ratio flux towers. *Remote Sens. Environ.* **2005**, *97*, 337–351.
51. Leclerc, M.Y.; Thurtell, G.W. Footprint prediction of scalar fluxes using a Markovian analysis. *Bound.-Lay. Meteorol.* **1990**, *52*, 247–258.
52. Bastiaanssen, W.G. SEBAL-based sensible and latent heat fluxes in the irrigated Gediz Basin, Turkey. *J. Hydrol.* **2000**, *229*, 87–100.
53. Twine, T.E.; Kustas, W.P.; Norman, J.M.; Cook, D.R.; Houser, P.R.; Meyers, T.P.; Prueger, J.H.; Starks, P.J.; Wesely, M.L. Correcting eddy covariance flux underestimates over a grassland. *Agric. For. Meteorol.* **2000**, *103*, 279–300.
54. Wilson, K.; Goldstein, A.; Falge, E.; Aubinet, M.; Baldocchi, D.; Berbigier, P.; Bernhofer, C.; Ceulemans, R.; Dolman, H.; Field, C.; *et al.* Energy balance closure at FLUXNET sites. *Agric. For. Meteorol.* **2002**, *113*, 223–243.
55. Hollinger, D.Y.; Richardson, A.D. Uncertainty in eddy covariance measurements and its application to physiological models. *Tree Physiol.* **2005**, *25*, 873–885.
56. Velpuri, N.M.; Senay, G.B.; Singh, R.K.; Bohms, S.; Verdin, J.P. A comprehensive evaluation of two MODIS evapotranspiration products over the conterminous United States: Using point and gridded FLUXNET and water balance ET. *Remote Sens. Environ.* **2013**, *139*, 35–49.
57. Thornton, P.E.; Running, S.W.; White, M.A. Generating surfaces of daily meteorological variables over large regions of complex terrain. *J. Hydrol.* **1997**, *190*, 214–251.

58. Mitchell, K.E.; Lohmann, D.; Houser, P.R.; Wood, E.F.; Schaake, J.C.; Robock, A.; Cosgrove, B.A.; Sheffield, J.; Duan, Q.; Luo, L.; *et al.* The multi-institution North American land data assimilation system (NLDAS): Utilizing multiple GCIP products and partners in a continental distributed hydrological modeling system. *J. Geophys. Res.* **2004**, doi: 10.1029/2003JD003823.

© 2013 by the authors; licensee MDPI, Basel, Switzerland. This article is an open access article distributed under the terms and conditions of the Creative Commons Attribution license (<http://creativecommons.org/licenses/by/3.0/>).